Star-Polymer Unimolecular Micelles for Brain Specific Delivery of Anticancer Drug

Mehak Malhotra
IISER Pune
Meenakshi Pardasani
IISER Pune
Priyadharshini Srikanth
IISER Pune https://orcid.org/0000-0002-5690-0089
Nixon Abraham
Indian Institute of Science Education and Research Pune https://orcid.org/0000-0001-8523-716X
Manickam jayakannan (jayakannan@iiserpune.ac.in)
IISER-Pune

Article

Keywords: Blood Brain Barrier, Block Copolymers, Drug Delivery, Imaging agents, Nanoparticles, and Fluorescent Probes

Posted Date: November 21st, 2022

DOI: https://doi.org/10.21203/rs.3.rs-2251762/v1

Abstract

Nanocarrier mediated therapeutic delivery to brain tissue remains an impediment by tightly controlled transportation across the blood brain barrier (BBB). Here, we report a well-defined core-shell star-shaped unimolecular micelle (star-UMM) based on biodegradable polycaprolactone platform as an efficient BBB breaching nanovector for brain specific administration of anticancer drug doxorubicin (DOX) and *in vivo* bioimaging via near-infrared biomarker IR780. The star-UMM was engineered by controlling the polymer topology of hydrophobic and hydrophilic segments from interior to exterior. *In vivo* imaging in mice was directly evident of prolonged blood circulation of star-UMM for more than 72 h, and the whole-organ image-quantification further substantiated its efficient BBB breaching ability. Star UMM having 15% of DOX exhibited excellent stability in blood circulation, reduction in cardiotoxicity, substantial uptake in the cortical neurons of mouse brain, lysosomal enzymatic-biodegradation, and negligible immunogenicity or necrosis; hence, proving the impact of the star UMM in brain-specific drug delivery.

Introduction

Drug delivery across the tightly regulated vasculature of the blood-brain barrier (BBB) in treating tumors and neurodegenerative diseases has been a major bottleneck.[1–3] The BBB maintains the homeostatic balance by regulating the transport of small-molecule nutrients and ions through the vasculature into the brain; thus, restricting the transportation of larger size and extraneous species across this biological barrier.[4] Nano-prodrug development has clearly identified that carriers having less than 50 nm size can penetrate the BBB and enable drug accumulation in brain.[5–9] Polypeptide nanoparticles (NPs),[10–13] protease-responsive-nanogels,[14] synthetic protein NPs,[15] self-assembled oligopeptide shuttles,[16–18] spherical nucleic acids,[19–20] albumin NPs,[21] pluoronic micelles,[22] chemotactic and chimeric polymerosomes,[23–24] liposomes,[25–26] dendrimers,[27–29] worm-like micelles,[30] T cell-medicated polymer NPs[31] are some of the important examples reported for BBB research. Uncontrollable glomerular renal filtration of the smaller (< 15 nm) nanocarriers, splenic and hepatic filtration of bigger NPs (> 200 nm) in the body limits the drug NP formulation concentration in the intravenous administration, which in turn reduces the bioavailability of NP for BBB crossing.[32–33] Thus, the next generation BBB crossing nanocarriers are mandatorily designed to be substantially stable to evade disassembly in body fluidics *in vivo*, tiny-size sub-nanometer objects (< 50 nm) for penetrating the tightly regulated t-junction, high drug loading content, reduced cardiotoxicity, and most importantly biodegradable for safe usage in BBB research.[34–38]

Among the many synthetic NPs, branched macromolecular architectures such as star block copolymers are known to exhibit resistance against renal filtration and retain the drug NP formulation in the blood for prolonged period.[33] Star-block copolymers provide excellent structural control to build well-defined core-shell nanoparticles.[39–41] Persistent to their three-dimensional globular core-shell geometry, star polymers often exist as unimolecular micelles[42–43] which is highly desirable for *in vivo* drug administration to maintain the drug NP against concentration gradient in the bloodstream. Here, these unique features of

the star-polymer unimolecular micelles (star-UMM) are explored for BBB research based on biodegradable polymer nanovector, for the first time, and the proof-of-concept was successfully demonstrated *in vivo* for clinically important anticancer drug doxorubicin (DOX) and brain-tissue penetrable near-infrared (NIR) biomarker IR-780. This new strategy is shown in Fig. 1.

Tweaking the topology of the macromolecular architectures was found to be very crucial factor in designing the star-UMM. For this purpose, hydrophobic polycaprolactone (PCL) and carboxylic substituted hydrophilic PCL segments were chosen based on our expertise in cancer research [44–53] and systematically several structures such as linear di-blocks, star di-blocks, and star random copolymers were tailor-made by ring opening polymerization (ROP) to get the right polymer geometry with high encapsulation capabilities. The *in vivo* biodistribution data established the supremacy of the star-UMM platform for crossing the BBB with reduced side-effect of cardiotoxicity. Further, microtubule assisted protein 2 (MAP 2), neuronal nuclei (NeuN) and glial fibrillary acidic protein (GFAP) immunostaining were employed to mark the different cell types across the brain tissue to ascertain the neural uptake of star-UMM.

Results And Discussion

Star-block copolymers were constituted with PCL core and -tert butyl ester substituted PCL segments at the periphery as shown in Fig. 2a employing an in-house built melt reactor (Supplementary Figure S1a) to perform solvent-free ring opening polymerization (ROP). Three star-polymers were synthesized in a sequential ROP process in which initial polymerization of ε-caprolactone (CL) yielded a 6-arm PCL macroinitiator (MI) having statistically 5, 10 and 20 units per arm. These PCL MI were subsequently employed for the ROP of t-butyl ester substituted caprolactone monomer[49] (*t*-BECL, Supplementary Figure S1b) (Fig. 2a and Supplementary Figure S1c) to yield three star-di-block polymers having 35/35, 60/60 and 120/120 units. For instance, the 60/60 diblock has 10 PCL units and 10 t-butyl ester PCL units per arm. The star block copolymers (SB) are referred to as SB-35, SB-60 and SB-100 where the number represents the total content of carboxylic ester substituted PCL segments at the periphery as shown schematically in Supplementary Figure S1d. To determine the structure and degree of polymerization (number of units), the peak intensities in ^{1}H-NMR were analysed in detail (Supplementary Figures S2 and S3). For feed [M]/[PCL MI] = 60, the actual incorporation was determined to be 64 ± 3 repeating units confirming the statistical distribution of 10 units per arm in the second block (Supplementary Figure S2a). Deprotection of t-butyl ester in these star block copolymers yielded their carboxylic acid substituted PCL block copolymers (^{1}H-NMR, Supplementary Figures S2 and S3). Size exclusion chromatography (SEC) was employed to determine the M_n, M_w and polydispersity index (PDI) and the values are summarized in table in Fig. 2b (SEC plots, Supplementary Figure S3b). Star-block copolymers were produced in very high molecular weights of 40 to 60 kDa which are sustainably enough to fold or self-assemble into a single polymer entity. Thermal properties of these new star polymers are in described in Supplementary Figure S3c.

Hydrophilic carboxylic PCL units in the periphery and hydrophobic PCL units in the core provided perfect molecular geometry for the star polymers to acquire required amphiphilicity. Star block copolymers were self-assembled by dialysis method (details in the experimental section). Dynamic light scattering (DLS) analysis determined the hydrodynamic diameter (D_h) of the star-block copolymer SB-60 to be D_h = 25 ± 7 nm (Fig. 2c). In Fig. 2c, FESEM and AFM images revealed the formation of spherical nanoparticles with average sizes of 23 ± 3 nm and 22 ± 5 nm, respectively. HR-TEM images were in coherence and histogram generated (not shown) from ~ 50 particles gave an average value of 24 ± 4 nm. From this data, the hydrodynamic radius (R_h) of the SB-60 NP was estimated to be 12 ± 3 nm. Small-angle X-ray scattering (SAXS) was employed to determine the radius of gyration (R_g) of SB-60, and based on the Guinier approximation, the R_g was estimated to be 7.1 ± 2.3 nm (Supplementary Figure S4a). The ratio of R_g/R_h was estimated to be 0.77 with respect to the existence of unimolecular micellar formulation.[54] Pyrene encapsulation study showed no change in the ratio of I_1/I_3 at different polymer concentrations depicting the unimolecular micelle self-assembly by the star-block copolymer SB-60 and SB-100 (Supplementary Figure S4b). SB-35 was not readily dispersable in water and produced turbid solution rendering it unusable. The above analysis is evident for the existence of core-shell < 30 nm sized star-UMMs by both SB-60 and SB-100.

Encapsulation capabilities of star-UMM NPs were studied for doxorubicin (DOX) and NIR dye IR780 by the dialysis method (experimental section). The DLC for SB-60, SB-100, SB-35 was obtained as 14.2%, 13.1% and < 1% for DOX, respectively (Fig. 2d). This suggested that SB-60 exhibited the most optimized core-shell structure to attain the highest DLC for star-UMM. The SB-35 does not have sufficient compartmentalization for DOX loading. The core-shell geometry probably attained maximum packing at SB-60; thus, no significant DLC increase was observed in SB-100. Encapsulation of NIR dye IR780 in SB-60 showed a very good DLC of 5% which is excellent for deep-tissue bioimaging analysis. The sizes of nascent and DOX-loaded star block copolymer formulations have been tabulated in Fig. 2b (DLS plots in Supplementary Figure S4c). All the nano-formulations showed monomodal size distribution with narrow PDI values. The IR780-loaded star block copolymer SB-60 analogue exhibited size in the range of 120 ± 10 nm. The zeta potential for nascent and DOX-loaded micelles was determined in the range of -3 mV to -26 mV (Fig. 2b), which implies the formation of neutral to slightly negatively charged nano-formulations.

To rationalize the role of topology of the star-block copolymer architectures towards its ability to self-assemble into unimolecular micelles in aqueous medium; two controlled molecules were made having linear di-block (LB-60) and star-random copolymer (SR-60, no segregation of core and shell) architectures. The chemical compositions and molecular weights of the SB-60, LB-60 and SR-60 are identical and they differ only by the arrangements of repeating units (Supplementary Figure S5a). The SR-60 self-assembled as D_h = 30 ± 5 nm sized NP, similar to that of SB-60 (Supplementary Figure S5b). However, the linear di-block LB-60 exhibited the D_h to be 170 ± 10 nm with respect to the formation of large-sized aggregated micelle (FESEM and HR-TEM images in Supplementary Figure S5c). The pyrene encapsulation experiment in LB-60 showed a breakpoint with respect to critical micellar concentration at 1 µg/mL (Supplementary Figure S5c) as typically reported for aggregated micelles. The SR-60 and LB-60

exhibited DLC = 3% and 2% for DOX encapsulation which is almost 7-fold lower than that of SB-60 star-UMM (Fig. 2d). This reiterates the importance of polymer topology for producing UMM with high degree of drug loading, and star block copolymers seems to be the way forward.

Aliphatic polyester backbone in star-UMM makes them fully lysosomal enzymatic-biodegradable[49]. In the presence of horse-liver esterase enzyme (10 U), > 95% drug release was observed within 24 h (Fig. 3a). The enzymatic cleavage by α-Chymotrypsin (8 U) resulted in release of only 60% DOX molecules. In the control, percentage release was substantially lower at a value of ~ 15%, indicating that the degradation of the UMM only occurred in the presence of lysosomal enzymes. The horse-liver esterase enzyme seemed to be the most suitable for complete degradation of the nano-assemblies. To determine the cyto-compatibility of these nanocarriers, MTT assay was employed in WT-MEF cell lines. Various concentrations of the nascent star block copolymer scaffold SB-60 were incubated with WT-MEF cells for 72 h (Supplementary Figure S6a). As is evident from the histogram, the polymer scaffold displayed 100% biocompatibility up to 100 µg/mL, and about 70–80% of cells were viable up to 200–500 µg/mL. Further, the cytotoxicity of the DOX-loaded scaffold SB-60 + DOX showed that the free DOX was more toxic to cells compared to their delivery from the polymer platform (Fig. 3b). CLSM images in Fig. 3c captured for cells incubated with free DOX and SB-60 + DOX unimolecular micelle are shown for the 180 min time point (live cell). The lysotracker staining helped to visualize the uptake of nanoparticles by the cells and co-localization of the DOX signal at lysosomal compartments. The signals from lysotracker (green) and DOX (red) can be seen as yellow in the merged image. This trend attributes that the star-nanocarrier is readily taken up by the cells via endocytosis and internalized at the lysosomal compartment for biodegradation. A control experiment with free DOX (in Fig. 3c and other time points in Supplementary Figure S6b) exhibited no colocalization with lysotracker, indicating that DOX being a small molecule, is taken up by the cells via diffusion.

NIR dye IR780, having excitation in the near-infrared region, overcomes the limitation of tissue auto-fluorescence whilst offering the advantage of deeper tissue penetration.[55] Two groups of mice (n = 3) were used; mice injected with free IR780 iodide dye (group 1) and SB-60 + IR780 (group 2) were utilized along with a control mouse (injected with 1X PBS) for *in vivo* biodistribution using the In Vivo Imaging System (IVIS, PerkinElmer). The IVIS imaging for tracking the biodistribution was carried out at 24 h, 48 h and 72 h, as can be seen in Fig. 3d (dorsal view). Using the dorsal view images of the mice, an attempt was made to quantify the IR780 distribution in the most rostral part of body with time across the two groups by selecting a region of interest (ROI). The plot of total radiant efficiency vs. time in Fig. 3e clearly demonstrated that the UMM SB-60 + IR780 exhibited superior potential to penetrate the BBB as opposed to the free dye and this distribution did not change with time up to 72 h. The plasma samples were also subjected to IVIS imaging to quantify the amount of IR780, the representative photographic image of the wells can be seen in Fig. 3f. The SB60 + IR780 nano-scaffolds demonstrated their ascendancy in their ability to be in circulation for longer duration than the free dye, (see plot of total flux vs. time in Fig. 3g). The *whole-organ* representative IVIS image for the brain captured at the 72 h time point can be seen in Fig. 3h. As can be seen from the average radiant efficiency plot, the SB-60 + IR780 unimolecular micelle

depicted higher uptake in the brain compared to free IR780 dye. The *whole-organ* imaging reiterated the ability of the SB-60 + IR780 star UMM to breach the BBB.

Having observed the brain specific uptake, the biodistribution and biochemical analysis of the DOX loaded star-UMM was investigated. A total of 19 mice of 8–12 weeks old female balb/c strain (~ 25 g in weight) for two experimental groups, 'free DOX' (group 1) and DOX loaded star-block copolymer 'SB-60 + DOX' (group 2) were utilized. Each group comprised of n = 6 mice; half of the mice (n = 3) were used for confocal imaging analysis of drug uptake by organs and histological analysis, while the other half (n = 3) were utilized for biochemical analysis to quantify the amount of DOX in each organ. To understand the biocompatibility of the polymers alone, an additional group (n = 6) was constituted as the control group, namely SB-60 (group 3), to confirm that the nascent polymer itself won't alter the physiology of the animal. As can be seen from Fig. 4a, for each mouse, the organs collected 24 h-post-injection were brain, heart, kidneys, liver, and spleen (see Supplementary Table ST1 for the organ weights). The DOX concentrations were determined and summarized in the bar diagram plot, as shown in Fig. 4b. An important observation was the significantly higher uptake of the SB-60 + DOX UMM in the brain tissue compared to free DOX. This was further closely investigated by measuring DOX biodistribution across brain regions under different conditions of delivering DOX. The % ID in the heart was the highest in case of free DOX, whereas the value for SB-60 + DOX was substantially lower. This is one of the highlights of our study considering the fact that the major side effect of chemotherapy with DOX is cardiotoxicity, and hence, reducing uptake of DOX in the heart by means of the nano-formulations would greatly overcome the toxic effects of the drug. The uptake by the liver, kidney and spleen tissues were almost similar across the two groups, with no significant difference. The DOX concentration was also determined in the plasma samples collected via retro-orbital plexus puncture at defined time points, and these values are shown in the Pharmacokinetics plot (Fig. 4c). The DOX concentration in plasma for the free DOX group was already less than half of the injected dose at the initial time point, thus their half-life could not be determined. The $t_{1/2}$ for the SB-60 + DOX group was determined to be 3.5 h using the non-compartmental analysis in the PK Solver software employing the log-linear trapezoidal method.

To study the immune response in the mice, the plasma samples collected from all the 19 mice (3 groups plus 1 mouse injected with 1X PBS as control) at 24 h time point were employed to determine the concentration of five cytokines, i.e., IL-2, IL-4, IL-17A, IFN- and TNF-α using the cytokine standard values. The mouse injected with PBS acts as the negative control, wherein no immune response is expected in the mouse since PBS is non-immunogenic. Across both groups, the cytokine expressions were very similar to that observed in the case of PBS, and the values were < 5 pg/mL (Supplementary Figure S6c), thereby suggesting that the nano-formulations were not immunogenic. Further hemolysis assay clearly exhibited the polymer biocompatibility with almost negligible hemolysis values at concentrations as high as 1000 μg/mL (Supplementary Figure S6d). Histological images of various organs upon SB-60 + DOX uptake via H&E staining are shown in Fig. 4d. The high-magnification images (40 X) obtained using a bright field microscope (Carl Zeiss) showed no signs of necrosis, blood clotting, or morphological alterations in any of the tissue samples for the SB-60 + DOX group. However, in the panel corresponding

to free DOX group some blood clotting was observed in the heart tissue, and according to the literature,[56] that is a sign of cardiotoxicity augmented by free DOX (see Supplementary Figure S7). Hence, the star block copolymer DOX loaded assemblies did not result in any damage to the tissues, unlike the free DOX.

The DAPI stained 50 μm sections were imaged to measure DOX uptake in brain and heart tissues across different groups, as shown in Figs. 4e (63 X) and Supplementary Figure S8 (63 X). Images from the kidney, liver, spleen, brain and heart (10 X) are shown in Supplementary Figure S8. In Fig. 4e, in the brain images, only SB-60 + DOX nano-formulation exhibited a strong red fluorescence signal (DOX) whereas, substantially low signal was observed in the free DOX group. This is attributed to the SB-60 + DOX UMM being 18–30 nm making them ideal nano-formulations to cross the BBB. These SB-60 + DOX micelles were able to passive selectively cross the BBB, accumulate in the brain tissue and these being stable at infinite dilution would not result in a premature drug release. Another brownie point for these SB-60 + DOX micelles was their ability to reduce the uptake in heart tissue, as can be seen from Supplementary Figure S8 of the heart tissue images. The signal of the SB-60 + DOX micelles was extremely weak compared to the strong red signal corresponding to free DOX. Thus, the current design of SB-60 UMM can overcome the aforementioned limitation and facilitates the use of even higher doses of DOX for chemotherapy in long term. The DOX uptake from the confocal images was quantified by determining the normalized mean gray values in Fig. 4f. These values for the SB-60 + DOX micelle exhibited enhanced uptake in the brain and drastically reduced uptake by the heart compared to an opposing trend in free DOX group. The renal clearance was higher in case of free DOX compared to the other group. The SB-60 + DOX exhibited reduced RES uptake, as can be seen from the low mean gray values in the liver and spleen tissues.

Quantifying the DOX intensities from the confocal images in Supplementary Figure S9 led to the interrogation of whether the nano-formulations were taken up equally by different parts of the brain tissue. Five different areas of the brain, namely cerebellum, amygdala, hippocampus, cortex, and olfactory bulb were used (posterior to anterior, see the labelling on the sagittal section of the mouse brain in Fig. 5a, adapted from the Gene Expression Nervous System Atlas).[57] The representative confocal images are shown in Supplementary Figure S9, and the DOX intensities visibly decreased upon going from the posterior part (cerebellum) to the anterior-most part (olfactory bulb). This was corroborated by the quantification of DOX intensities as normalized mean gray values plotted against the corresponding region of the brain (Fig. 5b). This trend can be attributed to the variation in the BBB heterogeneity and permeability across different brain regions, which depends on factors such as differential astrocyte and pericyte coverage, differences in tight-junction proteins like Zonula occludens (ZO)-1 and ZO-2, variation in cellular interactions between white and gray matter in different regions, changes in the vascular density, so on and so forth.[58] In order to examine the intracellular uptake of these micelles, immunostaining was carried out marking different brain tissue cell types, i.e., MAP 2 for staining the mature neurons, NeuN as the nuclei marker and GFAP for labelling the glial cells and astrocytes. The intent was to investigate the specificity of DOX loaded unimolecular micelles across the brain tissue, if any, and the results can be seen in Fig. 5c. The emission of DOX coming from within the mature neurons appeared to co-localize with the markers, as can be seen from the merged images (both 10 X-first column

and 63 X-second column) in Fig. 5c. This gave an affirmation of the intracellular uptake of the cargo and that uptake was similar across the brain tissue with no specificity for any cell type.

Mechanism illustrating the ability of the nano-scaffold to penetrate the BBB over the free drug has been outlined in Fig. 5d. The transcytosis across the barrier is dictated by factors such as lipophilicity, size, charge, molecular weight etc., and even with the requisite parameters the molecules are effluxed out into the blood stream via the P-glycoprotein (Pgp) pump.[59–61] The crucial parameters for nanoparticles intended to penetrate the BBB are their size < 50 nm, appropriate lipophilicity and surface charge is preferred to be near neutral.[59–61] In the current investigation, the plausible mechanism of BBB breach can be attributed to the caveolae-mediated transcytosis, that is known to transport albumin like macromolecules from the luminal side to brain parenchyma.[59–61] The crossing of the BBB by the star block copolymer UMM in the present study could be attributed to the following factors: i) prolonged blood circulation making it more bioavailable; ii) appropriate lipophilicity favourable for transcytosis and, iii) the presence of carboxylate groups on the periphery that circumvent the Pgp efflux pumps. All these factors combined with the sub-30 nm size range of the UMM could be the aid in breaching the BBB. To validate the ability of star block copolymer UMM to enter the neuronal cells upon crossing the BBB, an *in vitro* time-dependent experiment was envisaged. Herein, the SB-60 + DOX UMM were incubated with olfactory bulb (OB) and mixed cortical primary neuronal culture for 1 h and 4 h followed by immunocytochemistry and the panels are shown in Fig. 5e. DAPI and MAP 2 antibody staining was employed for imaging the differentiated mature neurons; represented via the blue (λ_{exc} = 405 nm) and green channels (λ_{exc} = 633 nm), respectively. The DOX emission (red channel, λ_{exc} = 488 nm) from the UMMs was observed to have substantial co-localization with the neuronal markers. The SB-60 + DOX uptake in both OB and cortical neurons was quantified and the plot of uptake (%) vs time depicted significantly higher uptake of SB-60 + DOX UMM in the cortical neurons as compared to the OB neurons across both the time points (Fig. 5e). The *in vitro* neuronal culture data was in coherence with the *in vivo* brain biodistribution data, wherein the UMM uptake was higher in the cortex as opposed to the OB (Fig. 5b). Taking cognizance of the *in vivo* and *in vitro* analysis, it can be stated that star-UMM demonstrated exceeding capability to breach the most tightly regulated biological barrier, i.e., the blood-brain barrier. Recent reports provide evidence for the role of synaptic signalling in the progression of brain tumours.[62,63] As expected from these results, sensory experience has been shown to modulate gliomagenesis, proven by regulating olfactory information processing in a mouse model.[64] These recent findings call for further experiments employing potential delivery systems combined with targeted delivery[65] and precise behavioural paradigms controlling sensory experiences.[66,67] Our results thus provide a potential drug delivery method for brain tumors adding significantly to the emerging field of “cancer neuroscience” research.[68,69]

Conclusion

New star-shaped biodegradable UMM was successfully design and developed via ROP methodology. Confocal microscopic analysis elucidated the internalization of DOX-loaded UMM at the lysosomal compartment and supported their enzymatic-biodegradation pathway of drug delivery. The star-block

copolymer UMM exhibited their ability to cross the BBB and accumulate in different cell types across multiple brain regions, as well as reduced the cardiotoxicity of DOX. The pharmacokinetics evaluation revealed a $t_{1/2}$ of 3.5 h for the star polymer, and the half-life could not be determined for free DOX due to their faster removal from the circulation. The biodistribution of the star-UMM was visualized in real-time by employing IVIS, that reiterated the potential of the UMM to penetrate the BBB to deliver dyes/drugs. The star polymer nano-formulations were non-immunogenic and biocompatible. The UMM uptake in the brain tissue was influenced by the BBB heterogeneity such that the uptake was higher in the posterior parts of the brain compared to the anterior section. MAP 2, NeuN and GFAP antibody staining confirmed a uniform DOX uptake across all brain tissue cell types. The *in vitro* primary neuronal culture data demonstrated enhanced uptake of the UMM by mixed cortical neurons. Hence, the current star-polymer design opens up opportunities for UMMs and successfully demonstrates their ability to penetrate the BBB *in vivo* to deliver drugs which could be useful for treatment of brain-related malignancies.

Methods

Synthesis of macro-initiators, star block copolymers, their structural characterization details, self-assembly and photophysical studies, drug encapsulation and *in vitro* drug release profiles, MTT assay are provided in the supporting information in detail.

Live cell imaging: The cellular uptake of free DOX and SB-60 + DOX was monitored with the aim of understanding the uptake mechanism and kinetics. To this effect, live cell experiment was devised with Lysotracker staining (stains the lysosomal compartment) in a time-dependent manner in WT-MEF cells. The 4-well live cell chamber plates were seeded with 25,000 cells per well in 1 mL of complete DMEM containing 10% FBS and 1% antibiotic followed by incubation at 5% CO_2 at a temperature of 37°C for 16 h. The requisite concentrations of free DOX and DOX loaded polymeric micelles (DOX concentration = 5 µg/ml) were added to separate wells and then incubated for three time points, i.e., 60, 90 and 180 min. At the end of the time point, the compound containing media was removed followed by addition of 50 nM lysotracker red DND-99 solution in DMEM and these were then imaged within 10 min using Leica SP8 while being incubated in a chamber maintained at 37°C and 5% CO_2 humidified atmosphere. The confocal imaging was done on a Leica SP8 system with a sequential scan setting using the lasers λ = 488 nm for DOX excitation and λ = 561 nm for excitation of the lysotracker red dye. The imaging analysis was done using Fiji software.

Mice handling and injection of nano-vehicles: Female balb/c mice of 8–12 weeks old (~ 25g in weight) were chosen for the *in vivo* experiments and these were divided into 3 groups of n = 6 each, namely free DOX, SB-60 + DOX, and SB-60. The aim behind the *in vivo* study was to unravel the effect of polymer topology on the biodistribution and pharmacokinetics parameters whilst comparing the same against the small molecule DOX, hence the two groups constituted were free DOX and SB-60 + DOX. The other group corresponded to nascent polymer scaffold as control to its DOX-loaded counterpart to help evaluate the immunogenicity and cytotoxic effects, if any, of polymer alone. One mouse was injected with PBS only without any compound; the organs and plasma procured from this mouse served as the control. For all

the experiments, the PBS, free DOX and all the nano-formulations were delivered using intraperitoneal injection. The DOX dosage for the biodistribution study was fixed at 2 mg/kg mice, which in this case translated to 50 µg DOX corresponding to 25 g mice and the concentration of DOX-loaded nano-formulations were determined using the drug loading content. Mice from group 1 were injected with 175 µL of DOX alone and group 2 mice were injected with 184 µL of unimolecular SB-60 + DOX. The aforementioned calculation helped us to determine the polymer amount required to inject 50 µg DOX and the same polymer concentration was injected into the mice in the nascent polymer group. Collection of blood sample was done from retro-orbital sinus, alternating between the sinuses during the sequential collection. Blood was collected at 2, 4, 8 and 24 h after the injection. Absorbable hemostatic gelatin sponge (AbGel) was used if the bleeding did not stop on its own. Animals were left undisturbed, maintained *ad libitum* in between the time points of blood collection. Mice were sacrificed at the end of 24 h post injection by transcardial perfusion and organs were collected to be further utilized either for biodistribution or biochemical analysis. All experimental mice were kept in individually ventilated cages in a temperature- and humidity- controlled animal facility and a 12-hours light/dark cycle was maintained in these rooms. All animal care and procedures were in accordance with the Institutional Animal Ethics Committee (IAEC) at IISER Pune and the Committee for the Purpose of Control and Supervision of Experiments on Animals (CPCSEA), Government of India.

Biochemical analysis of organs and blood samples: Blood sample was collected from each animal (all 3 groups) in heparin coated vials. For each time point, approximately 15 µL of blood was withdrawn from one of the retro-orbital sinuses. The blood was then centrifuged immediately for 20 minutes at 10000 rpm at 4°C to separate plasma from RBCs. The plasma in the supernatant was collected separately in new heparin coated vials and were stored at -80°C until the biochemical assay was carried out. After procuring all the plasma samples, DOX estimation per mL plasma was carried out. The main DOX stock solution was prepared [0.52 mg in 1.3 mL Cell lysis buffer (CLB)], and using this 10 different DOX concentrations were made in a 96-well plate maintaining the total volume to be 50 µL in order to generate a calibration plot. In each well of the 96-well plate, 5 µL of the plasma sample was taken followed by 45 µL of the cell lysis buffer (1:10 dilution) for n = 6 mice of group 1 (free DOX) and group 2 (SB-60 + DOX), and these were subjected to absorbance measurements at λ_{exc} = 487 nm using a microplate reader. Using the standard DOX curve, we quantified the amount of DOX (µg) per mL of plasma and determined the pharmacokinetics parameters. Brain, Heart, Liver, Kidneys and Spleen were obtained at 24-hour time point after the injection for the DOX containing 2 groups. Mice received Thiopentone injections intra-peritoneally (Thiosol sodium, Neon laboratories, 50mg/kg) to achieve deep anesthesia state. Mice then were decapitated and organs were dissected. The organs were blot dried using gauze, weighed, separately put in the vials, flash frozen in liquid nitrogen and then stored in cryo-boxes at -80°C until the biochemical assay was carried out. The organs were crushed using a mortar pestle in the presence of liquid nitrogen into a fine powder, followed by the addition of cell lysis buffer. These samples were brought to room temperature and dissolved in the buffer by pipetting. 50 µL of these tissue samples in CLB were aliquoted for further biochemical analysis. The aforementioned DOX standards were used for the assay and the calibration curve was generated by subjecting these samples to fluorescence

measurements (λ_{exc} = 487 nm, λ_{em} = 580 nm, excitation bandwidth = 12 nm) using a microplate reader. The aliquoted tissue samples were taken in a 96-well plate (5 µL) and diluted 10 times with 45 µL of CLB, then measured their fluorescence as per the previously mentioned settings. The amount of DOX (µg) per mg of the tissue was determined using the calibration curve and the weights of the organs were measured post dissection.

Histological analyses of organs: Histological analyses involved collection of organs of the 3 groups of mice. At 24 h time-point, mice received Thiopentone injections intra-peritoneally (Thiosol sodium, Neon laboratories, 50mg/kg) to achieve deep anesthesia state in order to carry out perfusion. Transcardial perfusion was done using 1X Phosphate buffered saline (PBS). Organs were dissected out and were put in separate 15 mL falcons filled with 4% Paraformaldehyde (PFA). Organs were kept immersed in 4% PFA at 4 °C for 24 h. They were then transferred to falcons filled with 0.0 % Sodium Azide in PBS (1X) and kept at 4 °C until required for the assays. To carry out Hematoxylin & Eosin (H&E) staining, 10 µm organ sections were taken on gelatin-formaldehyde coated glass slides in a cryotome. Before cryotomy, organs were further transferred to falcons filled with 0 % sucrose for 24–48 hours for cryo-preservation. Upon obtaining the sections, the slides were air-dried at 37 °C for 30 minutes before further processing was done. The solutions required for H&E staining were stored in Couplin jars kept at room temperature. Slides were moved through a sequential series of couplin jars containing Hematoxylin, Scott's tap water, Eosin, grades of alcohol (95%, 100%, 50% Xylene-50% alcohol) and 100% Xylene. Sections on slides were then mounted using DPX mountant (Thermo Fisher scientific) and stored at 4 °C before carrying out microscopy. The sections were imaged using bright field microscope (Carl Zeiss) to carry out qualitative analysis of any alterations in the tissue sections obtained from the organs of different groups of mice.

Quantification of biodistribution of Doxorubicin in organs using confocal microscopy: Organs were separately embedded in optimal cutting temperature (OCT) medium (Leica,14020108926) and sectioned at 50 µm thickness in a cryotome. Freely floating sections were collected at 300–350 µm intervals in 24 well/6-well plates, as per the requirement, filled with 1X PBS and stored at 4°C. DAPI (Sigma, 1:500 in 1X PBS) staining was carried out for a total of 5–6 sections per organ (approx. 300–350 µm apart). Sections were mounted on glass slides using Mowiol based aqueous mounting medium and stored at 4 °C until imaged. Confocal microscopy to image the amount of DOX in several field of views (FOVs) was carried out for 5 sections. Biodistribution quantification was done by calculating the mean gray value of the DOX intensity in the three groups of mice using Fiji Image J. The FOVs that were chosen for calculation were devoid of blood clots (checked using the DIC mode).

MAP 2, NeuN and GFAP Antibody staining: The 50 µm thick brain tissue sections of groups free DOX and SB-60 + DOX obtained via cryotome were subjected to MAP 2 antibody staining. For permeabilization and blocking, 2/3 large sections of the brain were added to a single well of a 24-well plate followed by addition of 250 µL of blocking solution (5% Normal goat serum (NGS) and 1% triton-X in 1X PBS) in each well and incubation at room temperature for 2 h. After the 2 h incubation, removed the blocking solution from each well. Added 1:1000 dilution of MAP 2 antibody (1 µL in 1 mL) in the blocking solution (1% NGS and 0.2% triton-X in 1X PBS), mixed well and then added 250 µL of this solution to each well. The plate

was then incubated on the shaker at 25 rpm for 20 h at 4°C, followed by three 1X PBS washes, wherein for each wash the plate was kept on the shaker at 25 rpm, room temperature for 15 min. After the third wash, the 1X PBS was inoculated from each well. The secondary antibody was added to the blocking solution (1% NGS in 1X PBS) in a 1:500 dilution (2 µL in 1 mL) and was thoroughly mixed before adding 250 µL in each well followed by incubation at room temperature for 2 h on the shaker at 25 rpm in the dark. After the incubation, wells were washed with 1X PBS thrice as mentioned before. This was followed by DAPI staining at1:500 dilution (2 µL in 1 mL) in the blocking solution (1% NGS in 1X PBS), 250 µL of this solution was added to each well, covered the plate with foil and kept on the shaker at 25 rpm for 10–12 mins at room temperature. The sections were mounted using the Vectashield mounting medium and stored at 4°C until imaged. Similar protocol was adopted for the NeuN and GFAP antibody staining of the 50 µm thick brain tissue sections of the SB-60 + DOX group.

Immunogenicity Analysis: The BD Cytometric Bead Array (CBA) Mouse Th1/Th2/Th17 Cytokine kit was employed to quantify the expression of cytokines, i.e., Interleukin (IL)-2, IL-4, IL-17A, Interferon-gamma (IFN-) and Tumor necrosis factor alpha (TNF-α) in the plasma samples corresponding to the 24 h time point for all the mice (n = 6) across the 3 groups and the one control mice injected with PBS. The plasma samples were thawed at 4°C for 2–3 h prior to the experiment. The lyophilized Mouse Th1/Th2/Th17 standard spheres were reconstituted with 2 mL of Assay diluent, referred to as the “Top standard”, equilibrated for ~ 15 min at room temperature followed by gentle mixing of the spheres (reconstituted protein) by pipetting. Serial dilutions were performed of the Top standard with the Assay Diluent in the ratios 1:2, 1:4, 1:8, 1:16, 1:32, 1:64, 1:128, 1:256 and one negative control was prepared containing only the Assay diluent. The next step was mixing of the five capture beads IL-2, IL-4, IL-17A, IFN- and TNF-α, wherein 10 µL of each capture bead for each assay tube was taken together and vortexed thoroughly. The plasma samples were diluted by the desired dilution factor (1:2, 1:10, 1:50 or 1:100) using the Assay diluent and then mixed thoroughly for the assay. The mixed capture beads were vortexed before adding 50 µL of the stock to each of the assay tubes (10 cytokine standards and plasma samples). To the control tubes, 50 µL of the cytokine standard dilutions were added such that the cytokine concentrations varied from 20 pg/mL (1:256 dilution) to 5000 pg/mL (Top standard). Further 50 µL of the plasma samples (diluted as mentioned above) were added to assay tubes containing the mixed capture beads. To all the assay tubes, 50 µL of the PE detection reagent was added followed by 2 h incubation at room temperature. Then 1 mL of wash buffer was added to all the assay tubes and centrifuged at 200 g for 5 min. The supernatant from each assay tube was decanted followed by addition of 300 µL wash buffer to each of the assay tube in order to resuspend the pellet. The samples were acquired on the BD Celesta (3 laser, 12 color) flow cytometer and analyzed using the FCAP Array software, wherein using the cytokine standard values the amount of each of the 5 cytokines was determined in all the plasma samples.

Hemolysis Assay: For the assay, blood sample (0.4 ml) was collected from C57B1/6 male mice (~ 9 weeks old) via the retro-orbital plexus puncture in heparin coated eppendorfs. The sample was centrifuged at 8000 rpm, room temperature for 10 min to separate the plasma from the red blood cells (RBCs). The supernatant plasma was discarded carefully leaving behind the RBCs and these were then washed with freshly prepared 1X PBS buffer thrice. Discarded the supernatant and diluted the RBCs using

1X PBS (5% v/v). 100 µL of this diluted RBCs stock was taken in a 96-well plate followed by addition of 100 µL of various polymer concentrations ranging from 10 µg/mL to 1000 µg/mL. PBS was chosen to be the negative control and Triton-X was the positive control required for the determination of % hemolysis. All the samples were recorded in triplicates. The 96-well plate was incubated at 37°C for an hour followed by centrifugation at 1400 rpm for 10 min. 100 µL of the supernatant was then transferred to another 96-well plate and the erythrocyte rupture was determined as a function of the amount of hemoglobin released by taking the absorbance read-out at 576 nm. Hemolysis (%) was determined using the formula

Hemolysis (%) = [(O.D.$_{576nm}$ in polymer sample - O.D.$_{576nm}$ in PBS)/(O.D.$_{576nm}$ in Triton-X - O.D.$_{576nm}$ in PBS)] X 100

IVIS mediated biodistribution analysis and whole-organ **imaging**: 12 weeks old female balb/c mice (~ 25g in weight) were chosen for the IVIS biodistribution study and these were divided into 2 groups of n = 3 each, namely free IR780 and SB-60 + IR780 along with a control mouse (injected with 1X PBS). The PBS, free IR780 and the nano-formulation were injected intra-peritoneally wherein the IR780 dosage was fixed at 0.5 mg/kg, that translated to 10 µg IR780 per mouse according to the body weight of ~ 25g. The dye loading content of SB-60 + IR780 was used to determine the exact concentration of the nano-formulation to be injected. Following the injections, blood samples were collected via retro-orbital plexus puncture at the time points 8h, 24 h, 48 h and 72 h. Absorbable hemostatic gelatin sponge (AbGel) was used in case the bleeding didn't stop. The biodistribution of the free IR780 dye and the SB-60 + IR780 UMM nano-formulation was monitored in real time by employing IVIS. Herein, the mice were imaged at time points 24 h, 48 h and 72 h while under anesthesia capturing both the dorsal and ventral view using the excitation and emission filter of λ_{exc} = 745 nm and λ_{em} = 820 nm. Mice were then sacrificed at the 72 h time point by cervical dislocation and the brain was procured in 1X PBS for *whole-organ* imaging analysis employing the same excitation and emission filters. Using the blood samples, plasma was isolated following the aforementioned procedure. The plasma samples obtained from n = 3 mice of the groups free IR780 and SB-60 + IR780 along with the control mouse (IX PBS) were inoculated in a 96-well plate at a 1:10 dilution (5 µL plasma sample + 45 µL cell lysis buffer). These samples were then subjected to the IVIS instrument analysis and the amount of the dye IR780 was determined by measuring the radiant efficiency at λ_{exc} = 745 nm.

Primary neuronal culture and immunocytochemistry: The olfactory bulb and cortex were dissected from postnatal day 1 C57/B6J mice pups and the tissues were minced in hanks balanced salt solution. The tissues were further digested using 0.25% Trypsin EDTA(1X) for 15 min at 37 ºC and neutralized with media containing serum. After multiple rounds of washes with wash buffer (HBSS containing 1% Pen Strep and 0.0033 M HEPES), the pellet was dissolved in Neurobasal medium supplemented with 10% fetal bovine serum, 1X B27 supplement, 0.25% L-Glutamine and 0.5% of Penicillin-streptomycin. The cells were seeded on a coverslip coated with poly-D-lysine. After 24 h, the culture was made serum free and the media was changed every three days. The SB-60 + DOX nanoparticle was dissolved in Neurobasal medium and the cells were incubated with the solution for 1 h and 4 h. The cells were fixed using 4% paraformaldehyde for 10 minutes and immunocytochemistry was performed. The cells were stained for

MAP2(Microtubule associated protein2) protein using Anti-chicken MAP2 antibody with 1:1500 dilution. Alexa Fluor chicken 647 antibody (1:500) was used as the secondary antibody and DAPI (1:500) was used for nuclear staining. The cells were then imaged using Leica SP8 and processed via the Fiji Image J software.

Statistics: All the analyses were done using Graphpad Prism 8.0 (Graphpad Software Inc, USA). Ordinary One-way ANOVA Turkey test and unpaired t-test were performed, and the values are represented as mean ± SEM.

Declarations

Data Availability

The authors declare that [the/all other] data supporting the findings of this study are available within the paper [and its supplementary information files].

Supporting Information

Synthesis, structural characterization and additional biological data are provided.

Acknowledgements

The authors thank research grant from Science and Engineering Research Board (SERB), Project No. CRG/2019/000496, New Delhi, INDIA, DBT/Wellcome Trust India Alliance intermediate grant (IA/I/14/1/501306 to N.A.), and DST-Cognitive Science Research Initiative (DST/CSRI/2017/271 to N.A.). We thank IISER Pune Microscopy Facility for cellular imaging. Part of the work was carried at the National Facility for Gene Function in Health and Disease (NFGFHD) at IISER Pune, supported by a grant from the Department of Biotechnology, Govt. of India (BT/INF/22/SP17358/2016).

Notes

Animal ethics committee approval number is IISER/IAEC/2018-02/07.

References

1. Banks, W.A. From blood-brain barrier to blood-brain interface: new opportunities for CNS drug delivery. *Nat. Rev. Drug Discov*. **15**, 275-292 (2016).
2. Ali, I. U. & Chen, X. Penetrating the blood-brain barrier: promise of novel nanoplatforms and delivery vehicles. *ACS Nano* **9**, 9470-9474 (2015).
3. Kreuter, J. Nanoparticulate systems for brain delivery of drugs. *Adv. Drug Delivery Rev.* **47**, 65-81 (2001).
4. Gastaldi, L., Battaglia, L., Peira, E., Chirio, D., Muntoni, E., Solazzi, I., Gallarate, M. & Dosio, F. Solid lipid nanoparticles as vehicles of drugs to the brain: Current state of art. *Eur. J. Pahrma. Biopharm.* **87**,

433-444 (2014).

5. Tang, W., Fan, W; Lau, J., Deng, L., Shen, Z. & Chen, X. Emerging blood-brain-barrier-crossing nanotechnology for brain cancer theranostics. *Chem. Soc. Rev*. **48**, 2967-3014 (2019).
6. Chen, Y. & Lu, L. Modern methods of delivery of drugs across the blood-brain barrier. *Adv. Drug Delivery Rev.* **64**, 640-665 (2012).
7. Z, Y., Peng, Z., Seven, E.S., & Leblanc, R.M. Crossing the blood-brain barrier with nanoparticles. *J. Control. Release.* **270**, 290-303 (2018).
8. Kreuter, J. Drug delivery to the central nervous system by polymeric nanoparticles: What do we know? *Adv. Drug Delivery Rev.* **71**, 2-14 (2014).
9. Wohlfart, S., Gelperina, S. & Kreuter, J. Transport of drugs across the blood-brain barrier by nanoparticles. *J. Control. Release.* **161**, 264-273 (2012).
10. Anraku, Y., Kuwahara, H., Fukusato, Y., Mizoguchi, A., Ishii, T., Nitta, K., Matsumoto, Y., Toh, K., Miyata, k., Uchida, S., Nishina, K., Osada, K., Ikata, K., Nishiyama, N., Mizusawa, H., Yamasoba, T., Yokota, T. & Katoaka, K. Glycaemic control boosts glucosylated nanocarrier crossing the BBB into the brain. *Nat. Commun.* **8**, 1001 (2017).
11. Liu, Y., Zou, Y., Feng, C., Lee, A., Yin, J., Chung, R., Park, J. B., Rizos, H., Tao, W., Zheng, M., Farokhzad, O. C. & Shi, B. Charge conversional biomimetic nanocomplexes as a multifunctional platform for boosting orthotopic glioblastoma RNAi therapy. *ACS Nano* **20**, 1637-1646 (2020).
12. Xie, J.; Gonzalez-Carter, D., Tockary, T.A., Nakamura, N., Xue, Y., Nakakido, M., Akiba, H., Dirisala, A., Liu, X., Toh, K., Yang, T., Wang, Z., Fukushima, S., Li, J., Quader, S., Tsumoto, K., Yokota, T., Ankraku, Y. & Kataoka, K. Dual-sensitive nanomicelles enhancing systemic delivery of therapeutically active antibodies specifically into the brain. *ACS Nano* **14**, 6729-6742 (2020).
13. Cabral, H.; Matsumoto, Y., Mizuno, K., Chen, Q., Murakami, M., Kimura, M., Terada, Y., Kano, M. R., Miyazono, K., Uesaka, M., Nishiyama, N. & Kataoka, K. Accumulation of sub-100 nm polymeric micelles in poorly permeable tumours depends on size. *Nat. Nanotechnol.* **6**, 815-823 (2011).
14. Singh, S., Drude, N., Blank, L., Desai, P. B., Konigs, H., Rutten, S., Langen, K., Moller, M., Mattaghy, F. M. & Morgenroth, A. Protease responsive nanogels for transcytosis across the blood-brain barrier and intracellular delivery of radiopharmaceuticals to brain tumour cells. *Adv. Healthcare Mater.* **10**, 2100812 (2021).
15. Alghamri, M. S., Banerjee, K., Mujeeb, A. A., Mauser, A.; Taher, A., Thalla, R., McClellan, B. L., Varela, M. L., Stamatovic, S. M., Martinez-Revollar, G., Andjelkovic, A. V., Gregory, J. V., Kadiyala, P., Calinescu, A., Jiménez, A. J., Apfelbaum, A. A., Lawlor, E. R., Carney, S., Comba, A., Faisal, S. M., Barissi, M., Edwards, M. B., Appelman, H., Sun, Y., Gan, Y., Ackermann, R., Schwendeman, A., Candolfi, M., Olin, M. R., Lahann, J., Lowenstein, P. R. & Castro, M. G. Systemic delivery of an adjuvant CXCR4-CXCL12 signaling inhibitor encapsulated in synthetic protein nanoparticles for Glioma immunotherapy. *ACS Nano* **16**, 8729-8750 (2022).
16. Diaz-Perlas, C., Oller-Salvia, B., Sanchez-Navarro, M., Teixido, M. & Giralt, E. Branched BBB-shuttle peptides: chemoselective modification of proteins to enhance blood-brain barrier transport. *Chem.*

Sci. **9**, 8409-8415 (2018).

17. Prades, R., Oller-Salvia, B., Schwarzmaier, S. M., Selva, J., Moros, M., Balbi, M., Grazu, V., de La Fuente, J. M., Egea, G., Plesnila, N., Teixido, M. & Giralt, E. Applyig the retro-enantio approach to obtain a peptide capable of overcoming the blood-brain barrier. *Angew. Chem. Int. Ed.* **54**, 3967-3972 (2015).
18. Arranz-Gilbert, P., Guixer, B., Malakoutikhah, M., Muttenthaler, M., Guzman, F., Teixido, M. & Giralt, E. Lipid bilayer crossing-the gate of symmetry. Water-soluble phenylproline-based blood-brain shuttles. *J. Am. Chem. Soc.* **137**, 7357-7364 (2015).
19. Bousmail, D., Amrein, L., Fakhoury, J.J., Fakin, H. H., Hsu, J. C. C., Panasci, L. & Sleiman, H. F. Precision spherical nucleic acid for delivery of anticancer drugs. *Chem. Sci.* **8**, 6218-6229 (2017*)*.
20. Xiao, F., Lin, L., Chao, C., Shao, C., Chen, Z., Wei, Z., Lu, J., Huang, Y., Li, L., Liu, Q., Liang, Y. & Tian, L. Organic spherical nucleic acids for the transport of NIR-II-emitting dye across the blood-brain barrier. *Angew. Chem. Int. Ed.* **59**, 9702-9710 (2020).
21. Lin, T., Zhao, P., Jiange, Y., Tang, Y., Jin, H., Pan, Z., He, H., Yang, V. C. & Huang, Y. Blood-brain-barrier-penetrating albumin nanoparticles for biomimetic drug delivery via albumin-binding protein pathways for antiglioma therapy. *ACS Nano* **10**, 9999-10012 (2016).
22. Khalin, I., Heimburger, D., Melnychuk, N., Collot, M., Groschup, B., Hellal, F., Reisch, A., Plesnila, N. & Klymchenko, A. S. Ultrabright fluorescent polymeric nanoparticle with a stealth Pluronic shell for live tracking in the mouse brain. *ACS Nano* **14***,* 9755-9770 (2020**)**.
23. Jiang, Y., Zhang, J., Meng, F. & Zhong, Z. Apolipoprotein E peptide-directed chimeric polymersomes mediate an ultrahigh-efficiency targeted protein therapy for glioblastoma. *ACS Nano* **12**, 11070-11079 (2018).
24. Joseph, A., Contini, C., Cecchin, D., Nyberg, S., Ruiz-Perez, L., Gaiztzsch, J., Fullstone, G., Tian, X., Azizi, J., Preston, J., Volpe, G. & Battaglia, G. Chemotactic synthetic vesicles: design and application in blood-brain barrier crossing. *Sci. Adv.* **3**, e1700362 (2017**)**.
25. Shi, D., Mi, G., Shen, Y. & Webster, T. J. Glioma-targeted dual functionalized thermosensitive ferri-liposomes for drug delivery through an *in Vitro* blood-brain barrier. *Nanoscale* **11**, 15057-15071 (2019).
26. Lundy, D. J., Lee, K-J., Peng, I-C., Hsu, C-H., Lin, J-H., Chen, K-H., Tien, Y-W. & Hsieh, P. C. H. Inducing a transient increase in Blood-brain barrier permeability for improved liposomal drug therapy of glioblastoma multiforme. *ACS Nano* **13**, 97-113 (2019).
27. Leiro, V., Santos, S. D., Lopes, C. D. F. & Pego, A. P. Dendrimers as powerful building blocks in central nervous system disease: headed for successful nanomedicine. *Adv. Funct. Mater.* **28**, 1700313 (2018).
28. Sharma, A., Sharma1, R., Zhang, Z., Liaw, K., Kambhampati, S. P., Porterfield J. E., Lin, K. C., DeRidder, L. B., Kannan, S. & Kannan, R. M. Dense hydroxyl polyethylene glycol dendrimer targets activated glia in multiple CNS disorders. *Sci. Adv.* **6**, eaay8514 (2020).
29. Sharma, A., Liaw, K., Sharma, R., Spriggs, T., Appiani La Rosa, S., Kannan, S. & Kannan, R. M. Dendrimer mediated targeted delivery of Rapamycin to tumour-associated macrophages improves

systemic treatment of glioblastoma. *Biomacromolecules* **21**, 5448-5161 (2020).

30. Zeng, L., Zou, L., Yu, H., Cao, H., Zhang, Z., Yin, Q., Zhang, P., Gu, W., Chen, L. & Li, Y. Treatment of malignant brain tumor by tumor-triggered programmed wormlike micelles with precise targeting and deep penetration. *Adv. Funct. Mater.* **26**, 4201-4212 (2016).
31. Ayer, M., Schuster, M., Gruber, I., Blatti, C., Kaba, E., Enzmann, G., Burri, O., Guiet, R., Seitz, A., Engelhardt, B. & Kloak, H-A. T cells-mediated transport of polymer nanoparticles across the blood-brain barrier. *Adv. Healthcare. Mater.* **10**, 2001375 (2021).
32. Choi, H. S., Liu, W., Misra, P., Tanaka, E., Zimmer, J. P., Ipe, B. I., Bawendi, M.G. & Frangioni, J. V. Renal clearance of quantum dots. *Nat. Nanotechnol.* **25**, 1165-1170 (2007).
33. Fox, M. E., Szoka F. C. & Frechet, M. J. Soluble polymer carriers for the treatment of cancer: The importance of molecular architecture. *Acc. Chem. Res.* **42**, 1141-1151 (2009).
34. Zhang, L., Yao, K., Wang, Y., Zhou, Y. L., Fu, Z., Li, G., Ling, J. & Yang, Y. Brain-targeted dual site selective platform for Nerve regeneration. *Nano. Lett*. **21**, 3007-3015 (2021).
35. Pahuja, R., Seth, K., Shukla, A., Shukla, R. K., Bhatnagar, P., Singh Chauhan, L. K., Saxena, P. K., Arun, J., Chaudhari, B. P., Patel, D. K., Singh, S. P., Shukla, R., Khanna, V. K., Kumar, P., Chaturvedi, R. K. & Gupta, K. C. Trans-Blood Brain Barrier Delivery of Dopamine-Loaded Nanoparticles Reverses Functional Deficits in Parkinsonian Rats. *ACS Nano* **9**, 4850-4871 (2015).
36. Guerrero-Cazares, H., Tzeng, S. Y., Young, N. P., Abutaleb, A. O., Quinones-Hinojisa, A. & Green, J. J. Biodegradable polymeric nanoparticles show high efficacy and specificity at DNA delivery to human Glioblastoma *in vitro* and *in vivo*. *ACS Nano* **8**, 5141-5153 (2014).
37. Wei, J., Xia, Y., Meng, F., Ni, D., Qiu, X. & Zhong, Z. Small, smart, and LDLR-specific micelles augment Sorafenib therapy of Glioblastoma. *Biomacromolecules* **22**, 4814-4822 (2021).
38. Clark, A. J. & Davis, M. E. Increased brain uptake of targeted nanoparticles by adding an acid-cleavable linkage between transferrin and the nanoparticle core. *Proc. Natl. Acad. Sci USA.* **6**, 12486-12491 (2015).
39. Yang, D-P., Linn Oo, M. N. N., Deen, G. R., Li, Z. & Loh, X. J. Nano-star-shaped polymers for drug delivery application. *Macromol. Rapid. Commun.* **38**, 1700410 (2017).
40. Ren, J. M., McKenzie, T. G., Fu, Q., Wong, E. H. H., Xu, J., An, Z., Shanmugam, S., Davis, T. P., Boyer, C. & Qiao, G. G. Star polymers. *Chem. Rev.* **116**, 6743-6836 (2016).
41. Wu, W., Wang, W. & Li, J. Star polymers: advances in biomedical application. *Prog. Polym. Sci*. **46**, 55-85 (2015).
42. Chen, G., Wang, Y., Xie, R. & Gong, S. A review on core-shell structured unimolecular nanoparticles for biomedical application. *Adv. Drug Delivery Rev.* **130**, 58-72 (2018).
43. Liu, H., Farrell, S. & Uhrich, K. Drug release characteristics of unimolecular polymeric micelles. *J. Control. Release*. **68**, 167-174 (2000).
44. Kulkarni, B., Malhotra, M. & Jayakannan, M. Fluorescent ABC-Triblock Polymer Nanocarrier for Cisplatin Delivery to Cancer Cells. *Chem. Asian J.* e202101337 (2022).

45. Ghosh, R., Malhotra, M., Madhuri Sathe, R.R. & Jayakannan, M. Biodegradable Polymer Theranostic Fluorescent Nanoprobe for Direct Visualization and Quantitative Determination of Antimicrobial Activity. *Biomacromolecules* **21**, 2896-2912 (2020).
46. Kulkarni, B., Malhotra, M. & Jayakannan, M. Perylene-Tagged Polycaprolactone Block Copolymers and Their Enzyme-Biodegradable Fluorescent Nanoassemblies for Intracellular Bio-Imaging in Cancer Cells. *ACS Appl. Polym. Mater.* **1**, 3375-3388 (2019).
47. Kulkarni, B. & Jayakannan, M. Fluorescent-Tagged Biodegradable Polycaprolactone Block Copolymer FRET Probe for Intracellular Bioimaging in Cancer Cells. *ACS Biomater. Sci. Eng.* **3**, 2185-2197 (2017).
48. Surnar, B. & Jayakannan, M. Triple Block Nanocarrier Platform for Synergistic Cancer Therapy of Antagonistic Drugs. *Biomacromolecules* **17**, 4075-4085 (2016).
49. Malhotra, M., Surnar, B. & Jayakannan, M. Polymer Topology Driven Enzymatic Biodegradation in Polycaprolactone Block and Random Copolymer Architectures for Drug Delivery to Cancer Cells. *Macromolecules* **49**, 8098-8112 (2016).
50. Surnar, B. & Jayakannan, M. Structural Engineering of Biodegradable PCL Block Copolymer Nanoassemblies for Enzyme-Controlled Drug Delivery in Cancer Cells. *ACS Biomater. Sci. Eng.* **2**, 1926-1941 (2016).
51. Kulkarni, B., Surnar, B. & Jayakannan, M. Dual Functional Nanocarrier for Cellular Imaging and Drug Delivery in Cancer Cells Based on π-Conjugated Core and Biodegradable Polymer Arms. *Biomacromolecules* **17**, 1004-1016 (2016).
52. Surnar, B., Sharma, K. & Jayakannan, M. Core-Shell Polymer Nanoparticles for Prevention of GSH Drug Detoxification and Cisplatin Delivery to Breast Cancer Cells. *Nanoscale* **7**, 17964-17979 (2015).
53. Surnar, B. & Jayakannan, M. Stimuli-Responsive Poly(caprolactone) Vesicles for Dual Drug Delivery under the Gastrointestinal Tract. *Biomacromolecules* **14**, 4377-4387 (2013).
54. Vagberg, L. J. M., Cogan, K. A. & Gast, A. P. Light-Scattering Study of Starlike Polymeric Micelles. *Macromolecules* **24**, 1670–1677 (1991).
55. Wang, L. & Niu, C. IR780-Based Nanomaterials for Cancer Imaging and Therapy. *J. Mater. Chem. B* **9**, 4079–4097 (2021).
56. Tang, H., Zhang, J., Tang, J., Shen, Y., Guo, W., Zhou, M., Wang, R., Jiang, N., Gan, Z. & Yu, Q. Tumor Specific and Renal Excretable Star-like Triblock Polymer-Doxorubicin Conjugates for Safe and Efficient Anticancer Therapy. *Biomacromolecules* **19**, 2849–2862 (2018).
57. Gong, S., Zheng, C., Doughty, M. L., Losos, K., Didkovsky, N., Schambra, U. B., Nowak, N. J., Joyner, A., Leblanc, G., Hatten, M. E. & Heintz, N. A Gene Expression Atlas of the Central Nervous System Based on Bacterial Artificial Chromosomes. *Nat.* **425**, 917–925 (2003).
58. Suciu, M., Hermenean, A. & Wilhelm, I. Heterogeneity of the Blood-Brain Barrier. No. March, 1–8 (2016).
59. Pulicherla, K. K. & Kumar Verma, M. Targeting Therapeutics Across the Blood Brain Barrier (BBB), Prerequisite Towards Thrombolytic Therapy for Cerebrovascular Disorders-an Overview and Advancements. https://doi.org/10.1208/s12249-015-0287-z.

60. Zhou, M., Shi, S. X., Liu, N., Jiang, Y., Karim, M. S., Vodovoz, S. J., Wang, X., Zhang, B. & Dumont, A. S. Caveolae-Mediated Endothelial Transcytosis across the Blood-Brain Barrier in Acute Ischemic Stroke. *J. Clin. Med.* **10,** (2021).
61. Ayloo, S. & Gu, C. Transcytosis at the Blood-Brain Barrier. *Curr. Opin. Neurobiol.* **57**, 32 (2019).
62. Venkataramani, V., Tanev, D. I., Strahle, C., Studier-Fischer, A., Fankhauser, L., Kessler, T., Körber, C., Kardorff, M., Ratliff, M., Xie, R., Horstmann, H., Messer, M., Paik, S. P., Knabbe, J., Sahm, F., Kurz, F. T., Acikgöz, A. A., Herrmannsdörfer, F., Agarwal, A., Bergles, D. E., Chalmers, A., Miletic, H., Turcan, S., Mawrin, C., Hänggi, D., Liu, H. K., Wick, W., Winkler, F. & Kuner, T. Glutamatergic Synaptic Input to Glioma Cells Drives Brain Tumour Progression. *Nature* **573**, 532–538 (2019).
63. Zeng, Q., Michael, I. P., Zhang, P., Saghafinia, S., Knott, G., Jiao, W., McCabe, B. D., Galván, J. A., Robinson, H. P. C., Zlobec, I., Ciriello, G. & Hanahan, D. Synaptic Proximity Enables NMDAR Signalling to Promote Brain Metastasis. *Nature* **573**, 526–531 (2019).
64. Chen, P., Wang, W., Liu, R., Lyu, J., Zhang, L., Li, B., Qiu, B., Tian, A., Jiang, W., Ying, H., Jing, R., Wang, Q., Zhu, K., Bai, R., Zeng, L., Duan, S. & Liu, C. Olfactory Sensory Experience Regulates Gliomagenesis via Neuronal IGF1. *Nature* **606**, 550–556 (2022).
65. Abraham, N. M., Egger, V., Shimshek, D. R., Renden, R., Fukunaga, I., Sprengel, R., Seeburg, P. H., Klugmann, M., Margrie, T. W., Schaefer, A. T. & Kuner, T. Synaptic Inhibition in the Olfactory Bulb Accelerates Odor Discrimination in Mice. *Neuron* **65**, 399–411 (2010).
66. Bhattacharjee, A. S., Konakamchi, S., Turaev, D., Vincis, R., Nunes, D., Dingankar, A. A., Spors, H., Carleton, A., Kuner, T. & Abraham, N. M. Similarity and Strength of Glomerular Odor Representations Define a Neural Metric of Sniff-Invariant Discrimination Time. *Cell Rep.* **28**, 2966-2978.e5 (2019).
67. Abraham, N. M., Guerin, D., Bhaukaurally, K. & Carleton, A. Similar Odor Discrimination Behavior in Head-Restrained and Freely Moving Mice. *PLoS One* **7**, 1–9 (2012).
68. Venkataramani, V., Tanev, D. I., Kuner, T., Wick, W. & Winkler, F. Synaptic Input to Brain Tumors: Clinical Implications. *Neuro. Oncol.* **23**, 23–33 (2021).
69. Monje, M., Borniger, J. C., D'Silva, N. J., Deneen, B., Dirks, P. B., Fattahi, F., Frenette, P. S., Garzia, L., Gutmann, D. H., Hanahan, D., Hervey-Jumper, S. L., Hondermarck, H., Hurov, J. B., Kepecs, A., Knox, S. M., Lloyd, A. C., Magnon, C., Saloman, J. L., Segal, R. A., Sloan, E. K., Sun, X., Taylor, M. D., Tracey, K. J., Trotman, L. C., Tuveson, D. A., Wang, T. C., White, R. A. & Winkler, F. Roadmap for the Emerging Field of Cancer Neuroscience. *Cell* **181**, 219–222 (2020**)**.

Figures

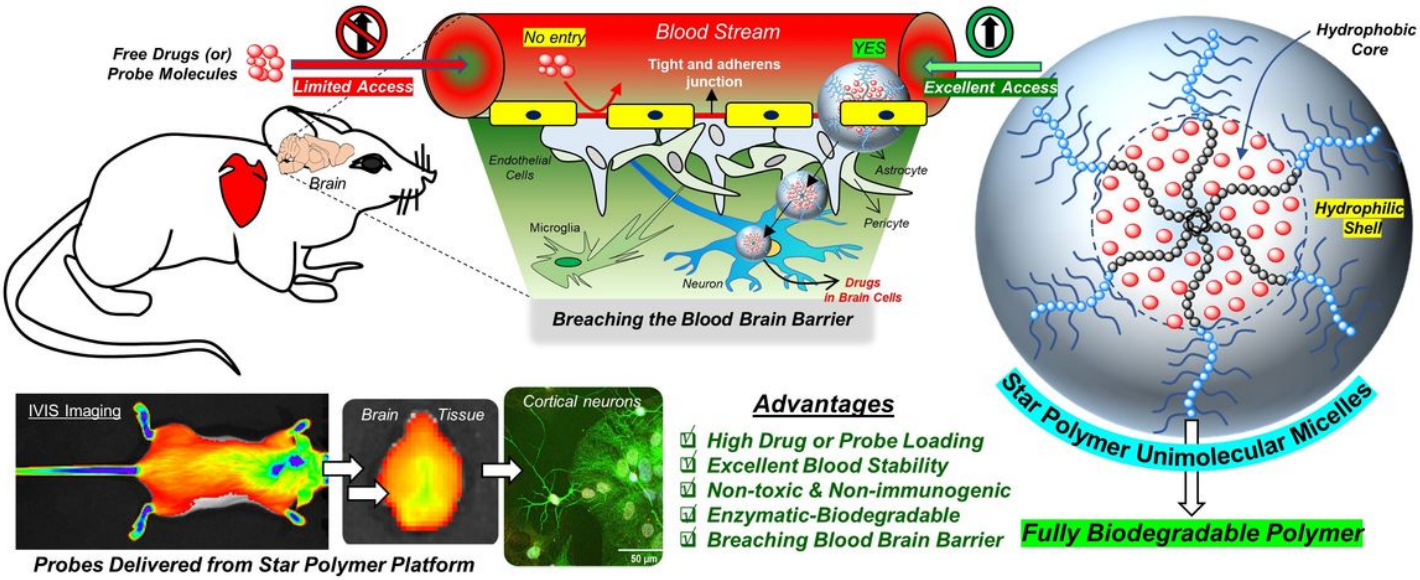

Figure 1

New Strategy for Blood Brain Barrier Breaching: *Design and development of biodegradable star block copolymer unimolecular micelles (UMM) for brain specific delivery*

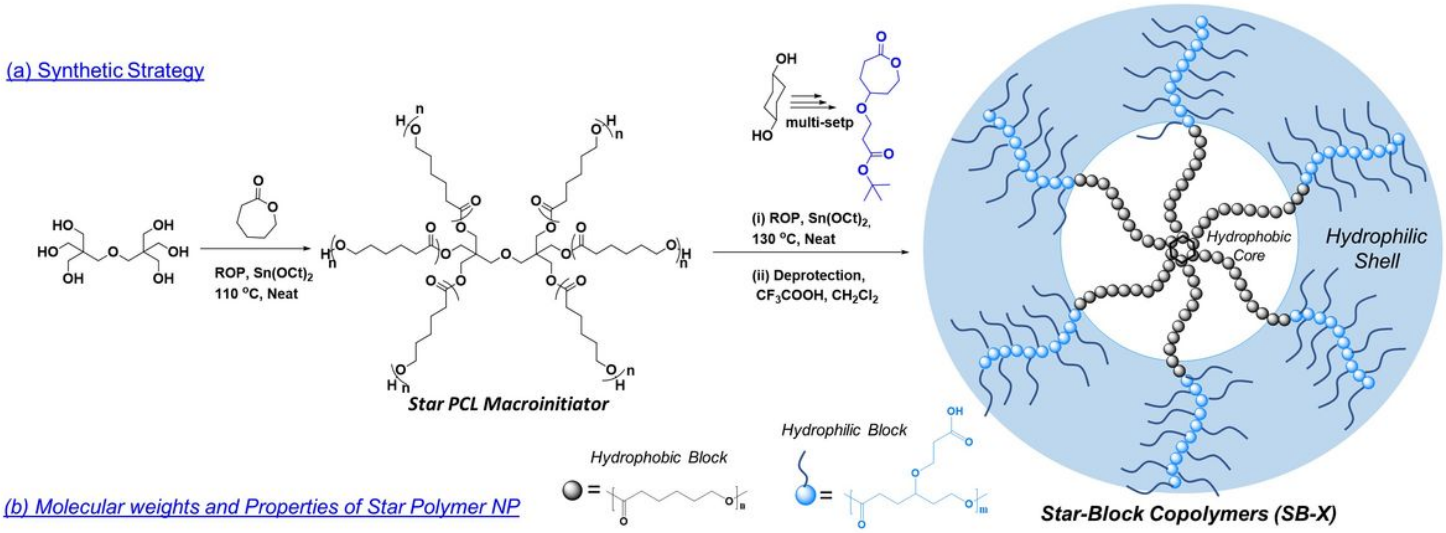

(b) Molecular weights and Properties of Star Polymer NP

Star PCL Macroinitiator	Star Block Copolymer	M_n (^{1}H NMR) (g/mol)	M_n (SEC) (g/mol)	M_w (SEC) (g/mol)	Đ	D_h (nm)	ξ (mV)	PDI	Sample	D_h (nm)	ξ (mV)	PDI
Nascent Star Nanoparticles									DOX Loaded Star Nanoparticles			
S-35	SB-35	13200	21300	36300	1.7	156 ± 2	-16.1	0.4	SB-35+DOX	135±7	-26.5	0.1
S-60	SB-60	25200	30200	42000	1.4	25 ± 7	-7.8	0.4	SB-60+DOX	23±2	-11.9	0.4
S-110	SB-100	38600	44800	60200	1.3	38 ± 6	-7.1	0.3	SB-100+DOX	37±2	-3.5	0.3

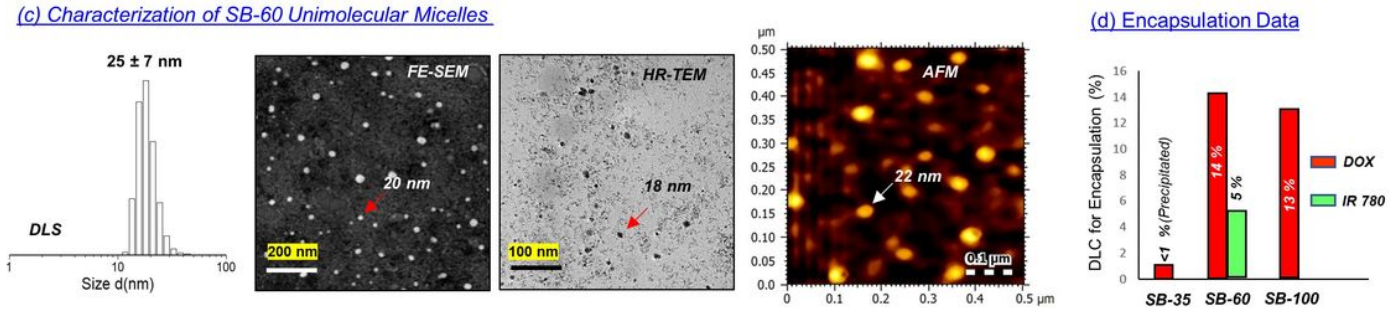

Figure 2

Synthesis and Characterizaton of Star Polymer Nanovector: *(a) Synthetic scheme of star block copolymers. (b) Table containing the molecular weights, hydrodynamic diameter of the polymers in self-assembled state in water and their DOX-loaded counterparts (concentration = 0.1 mg/mL), Zeta potential value, polydispersity. (c) FESEM, AFM and HR-TEM images were recorded at 0.05 mg/mL concentration in water. (d) Drug loading content (DLC) for doxorubicin and dye loading content (DLC) for IR780 in the nanoparticles.*

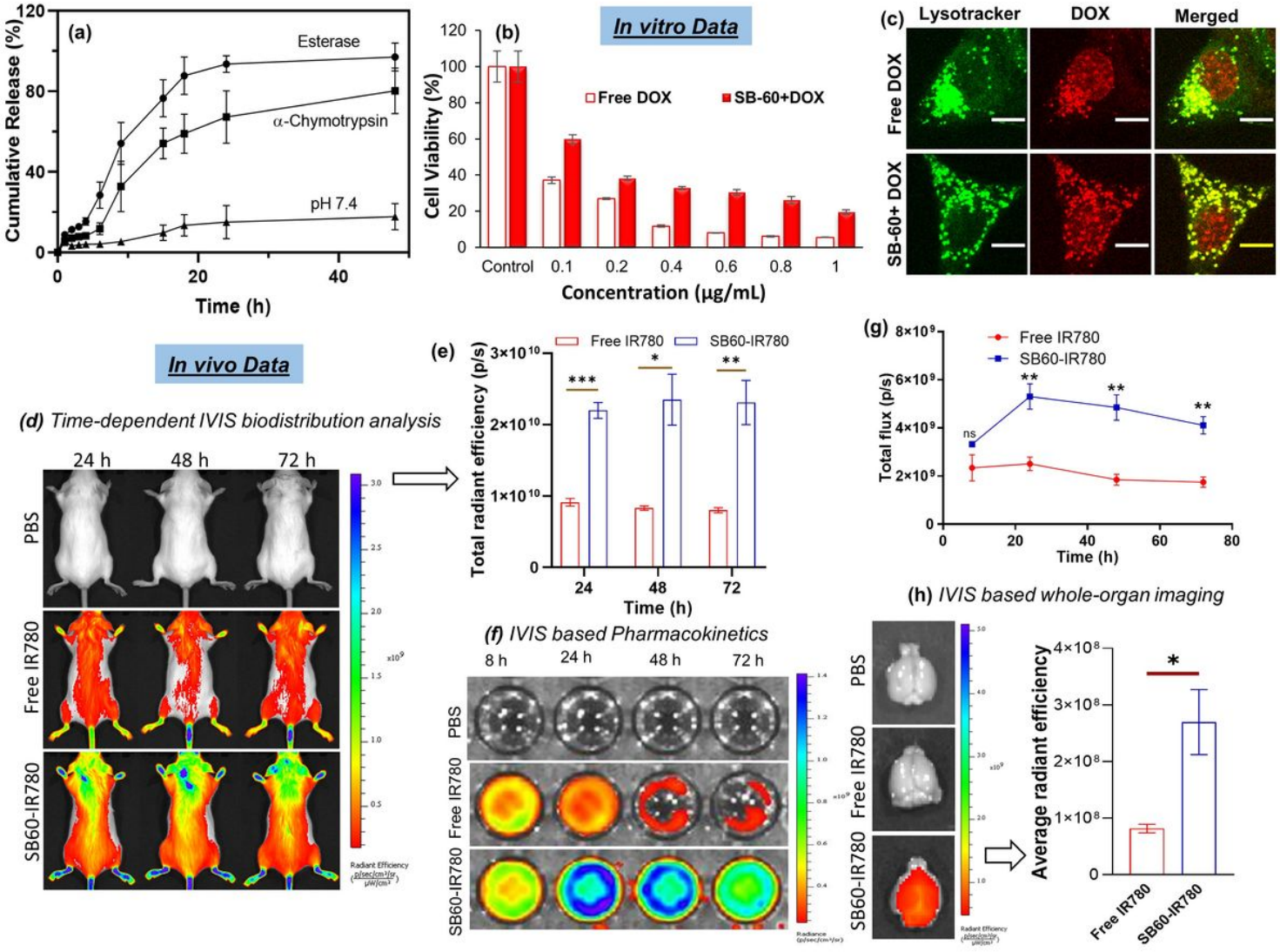

Figure 3

In vitro* Cellular Studies and IVIS Bioimaging Analysis:** *(a) In vitro DOX release kinetics (in hours) of SB-60+DOX nanoparticle in PBS alone and in presence of esterase (10U) and α-Chymotrypsin (8U) at pH 7.4 incubated at 37 °C (Concentration of SB-60+DOX nanoparticle = 1 mg/mL). (b) Cytotoxicity of free DOX and SB-60+DOX in WT-MEF cell lines at concentrations up to 1 µg/mL. (c) CLSM images of a live cell experiment carried out with free DOX and SB-60+DOX unimolecular micelle in WT-MEF cells (DOX concentration = 5 µg/mL, Incubation time = 180 min) and employed Lysotracker Red DND-99 to stain the lysosomes. DOX was excited using the 488 nm laser and the lysotracker excitation was done using the 561 nm laser (Scale bar = 10 mm). (d) Time-dependent IVIS mediated biodistribution analysis of free IR-780 and SB-60+IR780 UMM along with a control mouse injected with 1X PBS (Dorsal view). (e) Plot of total radiant efficiency vs. time quantifying the amount of dye IR780 in the most rostral body region. Each point represents mean ± SEM (n = 3) (P = 0.0005, * P = 0.0133, ** P = 0.0084). (f) Representative image of the plasma samples captured in a 96-well plate via IVIS. (g) Plot of total flux vs. time depicting the amount of IR780 dye in the plasma samples collected at different time points. Each point represents mean ± SEM (n = 3) (** P = 0.0096, ** P = 0.0063, ** P = 0.005). (h) IVIS based whole-organ imaging of*

the brain. Whole-organ image-based quantification represented as the plot of average radiant efficiency depicting the amount of dye IR780 in the brain tissue measured 72 h after injection, for free dye and SB-60+IR780. Each point represents mean ± SEM (n = 3) (P = 0.0315).*

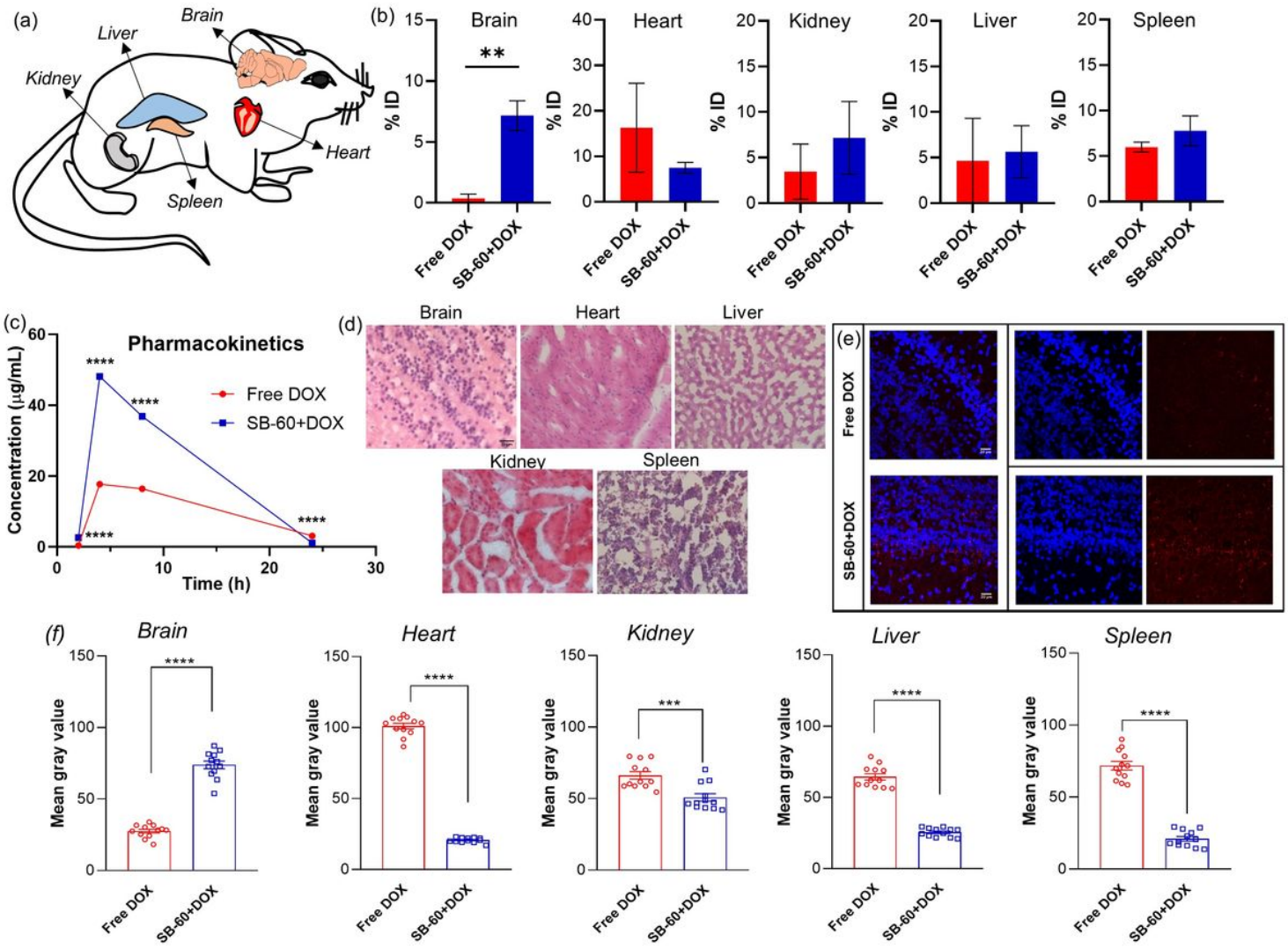

Figure 4

In vivo* Biodistribution Analysis of DOX loaded Star Nanovector:** *(a) Illustration of a mouse, transcardially perfused and the specified organs were dissected for carrying out biodistribution analysis. (b) Quantification of DOX in brain, heart, kidneys, liver and spleen for free DOX and SB-60+DOX represented as the % Injected dose (% ID). (** P = 0.0060) (c) Concentration of DOX in plasma for free DOX and SB-60+DOX. Each point represents mean ± SEM (n = 6) (* P < 0.0001). The error bars have been added to the plot, but because of the small values the bars are not visible. (d) H&E (Hematoxylin & Eosin) stained tissue samples for SB-60+DOX imaged at 40 X (Scale bar = 20 μm). (e) Immunofluorescence images depicting the uptake of free DOX and SB-60+DOX for the Brain tissue imaged at 63 X (scale bar = 50 μm). (f) Plot of normalized mean gray values representing the quantification of uptake of free DOX and SB-*

*60+DOX by the Brain, Heart, Kidney, Liver and Spleen tissue samples. Each point represents mean ± SEM (n = 12) (**** P < 0.0001, *** P = 0.001).*

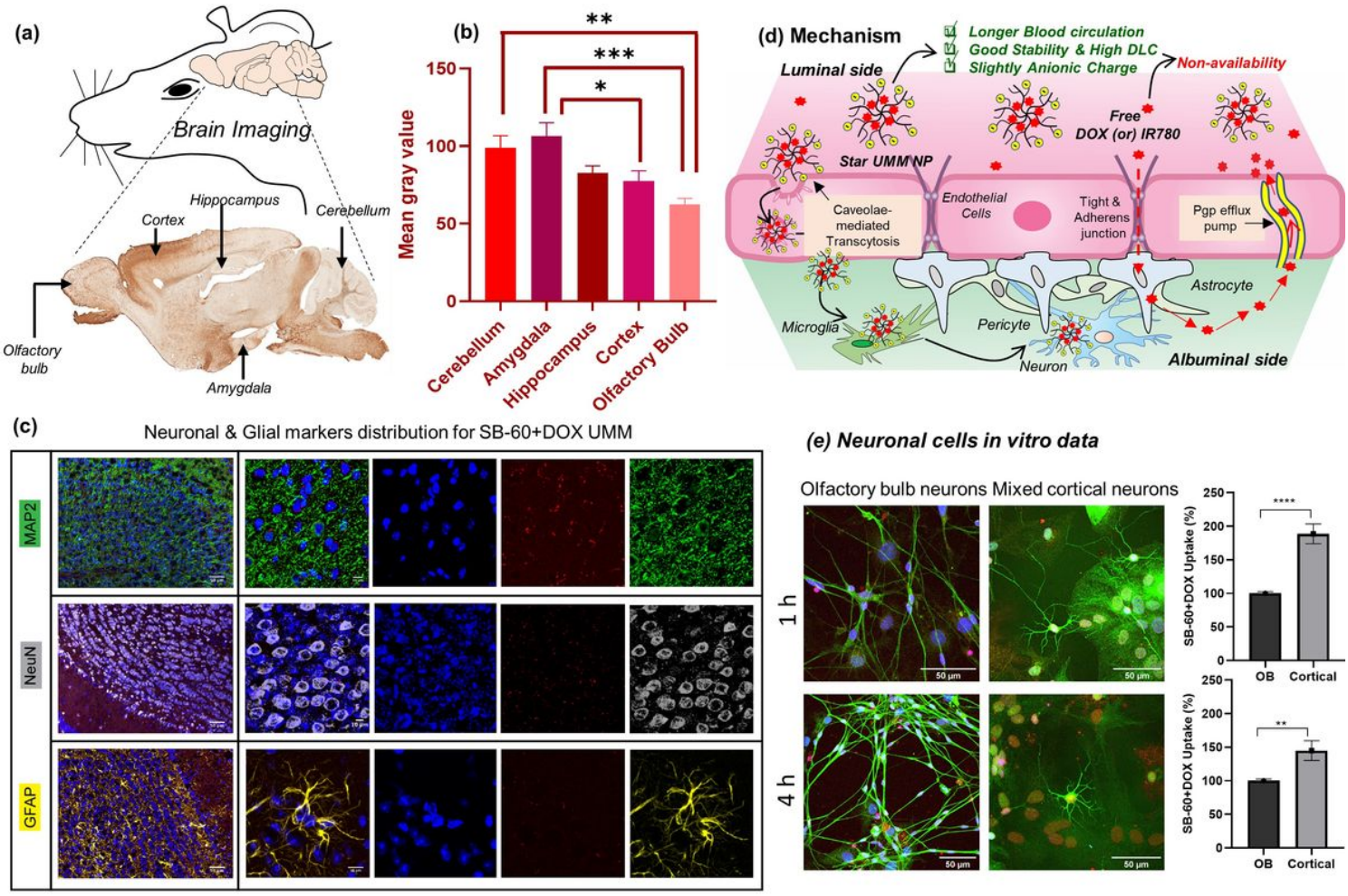

Figure 5

Brain Specific Delivery and Mechanism for BBB Crossing: *(a) Different areas of brain are marked which were utilized for SB-60+DOX uptake quantification, on the sagittal section (Lamp5 gene expression in a transgenic Cre mouse) of mouse brain adapted from the Gene Expression Nervous System Atlas (GENSAT). (b) Plot of normalized mean gray value compared across different regions of the brain tissue for the SB-60+DOX nanoparticle. Each point represents mean ± SEM (n = 10) (*** P = 0.0001, ** P = 0.0019, * P = 0.0208). (c) Immunofluorescence images (63 X) of the MAP 2, NeuN and GFAP stained neurons and glial cells in brain for SB-60+DOX nanoparticles. Scale bar = 10 µm. (d) Plausible mechanism illustrating the ability of the SB-60 UMM to breach the BBB over free drug. (e) In vitro primary neuronal culture time-dependent experiment representing uptake of SB-60+DOX in both olfactory bulb and mixed cortical neurons. Plot of uptake (%) vs. time across both neuronal cultures. Each point represents mean ± SEM (**** P < 0.0001, ** P = 0.0058).*

Supplementary Files

This is a list of supplementary files associated with this preprint. Click to download.

- TableOfContent.jpg
- SupportingInformation.docx